Nonvolatile and Programmable Photodoping in MoTe₂ for Photoresist-Free Complementary Electronic Devices

Tao Liu, Du Xiang,* Yue Zheng, Yanan Wang, Xinyun Wang, Li Wang, Jun He, Lei Liu, and Wei Chen*

2D transition-metal dichalcogenide (TMD)-based electronic devices have been extensively explored toward the post-Moore era. Huge efforts have been devoted to modulating the doping profile of TMDs to achieve 2D p–n junctions and inverters, the fundamental units in logic circuits. Here, photoinduced nonvolatile and programmable electron doping in MoTe₂ based on a heterostructure of MoTe₂ and hexagonal boron nitride (BN) is reported. The electron transport property in the MoTe₂ device can be precisely controlled by modulating the magnitude of the photodoping gate exerted on BN. Through tuning the polarity of the photodoping gate exerted on BN under illumination, such a doping effect in MoTe₂ can be programmed with excellent repeatability and is retained for over 14 d in the absence of an external perturbation. By spatially controlling the photodoping region in MoTe₂, a photoresist-free p–n junction and inverter in the MoTe₂ homostructure are achieved. The MoTe₂ diode exhibits a near-unity ideality factor of ≈1.13 with a rectification ratio of ≈1.7 × 10⁴. Moreover, the gain of the MoTe₂ inverter reaches ≈98, which is among the highest values for 2D-material-based homoinverters. These findings promise photodoping as an effective method to achieve 2D-TMDs-based nonvolatile and programmable complementary electronic devices.

2D transition-metal dichalcogenides (TMDs) are promising building blocks for the post-Moore electronic devices due to their extraordinary and unique properties.[1–8] Huge efforts have been devoted to modulating their carrier transport properties to realize unipolar n- and p-type field effect transistors (FET) for fundamental logic circuit units (e.g., p–n junction and inverter) in homogeneous 2D structure.[9–20] Surface charge transfer doping (SCTD), relying on the interfacial charge transfer between dopant and material, has been extensively investigated to tune the carrier transport properties of 2D TMDs.[11–16,18–20] The unipolar n- and p-type TMD FETs can be successfully achieved by selecting the corresponding dopants, which makes it possible to realize the homogeneous TMD p–n junction and inverter.[11,12,19,20] However, traditional SCTD technique is irreversible and nonprogrammable, that is, the doping effect in doped material cannot be written and erased at will. Moreover, by using traditional SCTD technique to realize the spatially controlled doping, photoresist and multistep lithography are generally unavoidable, which not only increases the fabrication complexity but may also degrade the device quality. Electrostatic gating has also been adopted to modulate the major carriers in ambipolar TMDs such as WSe₂ and MoTe₂, in which a homogeneous p–n junction can be obtained by coupling two split local gates.[21–24] Nevertheless, such p–n junction is unable to be maintained once the local gating is removed, suggesting its volatility. Nonvolatile and programmable photodoping effect has been observed in graphene FET through optical excitation of boron nitride (BN) in a graphene/BN heterostructure.[25] However, the absence of an intrinsic bandgap in graphene hinders its application in logic electronics. Taking the advantage

---

Dr. T. Liu, Dr. D. Xiang, Prof. W. Chen
Department of Chemistry
National University of Singapore
3 Science Drive 3, Singapore 117543, Singapore
E-mail: chmxdu@nus.edu.sg; phycw@nus.edu.sg

Y. Zheng, Y. Wang, X. Wang, Prof. W. Chen
Department of Physics
National University of Singapore
2 Science Drive 3, Singapore 117542, Singapore

Prof. L. Wang
Institute for Advanced Study and Department of Physics
Nanchang University
999 Xue Fu Da Dao, Nanchang 33003, P. R. China

The ORCID identification number(s) for the author(s) of this article can be found under https://doi.org/10.1002/adma.201804470.

Prof. J. He
School of Physics and Electronics
Central South University
932 South Lushan Road, Changsha 410083, P. R. China

Prof. L. Liu
State Key Laboratory of Luminescence and Applications
Changchun Institute of Optics
Chinese Academy of Sciences
No. 3888 Dongnanhu Road, Changchun 130033, P. R. China

Prof. W. Chen
Centre for Advanced 2D Materials and Graphene Research Centre
National University of Singapore
6 Science Drive 2, Singapore 117546, Singapore

Prof. W. Chen
National University of Singapore (Suzhou) Research Institute
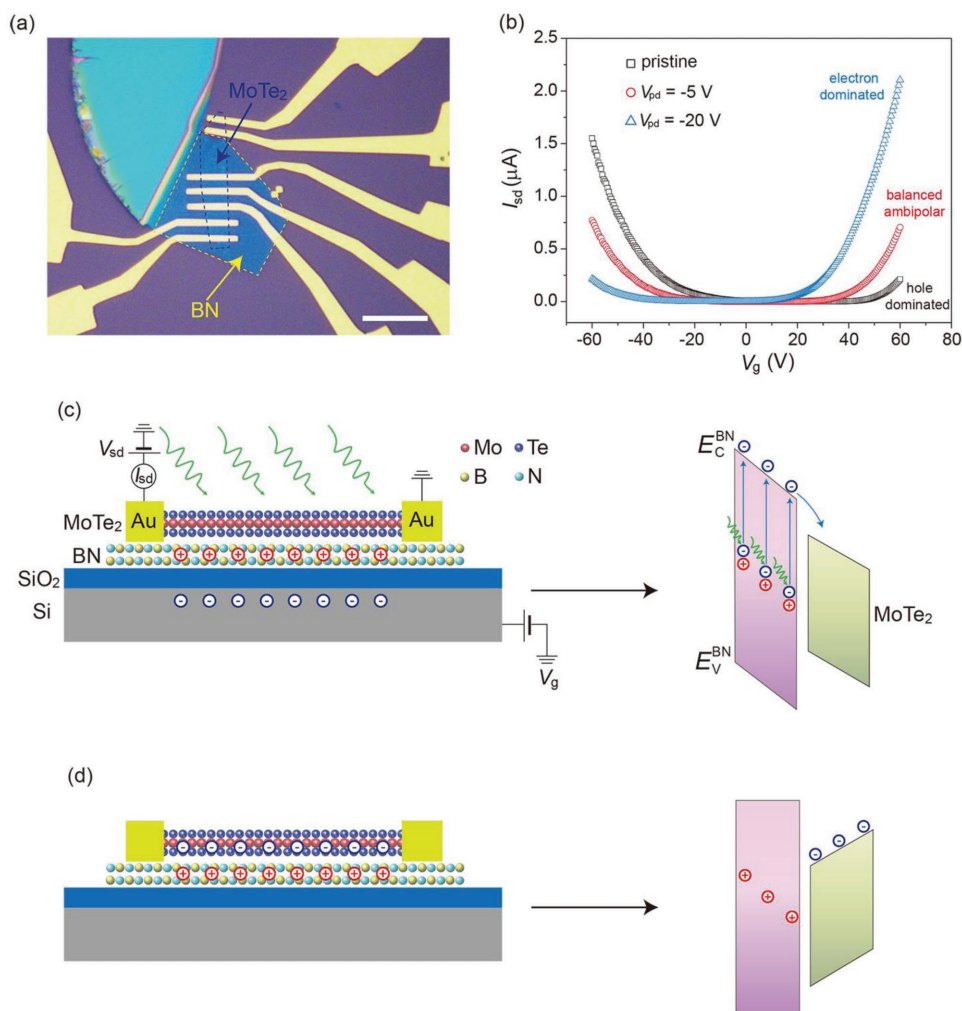377 Lin Quan Street, Suzhou Industrial Park
Jiang Su 215123, P. R. China

**ADVANCED
SCIENCE NEWS**

www.advancedsciencenews.com

**ADVANCED
MATERIALS**

www.advmat.de

Figure 1. a) Optical microscopy image of the fabricated MoTe$_2$ FET on BN flake. The scale bar is 10 µm. b) Linear plot of the transfer curves at photodoping gate $V_{pd} = -5$ and -20 V with respect to the pristine MoTe$_2$. The source–drain voltage $V_{sd} = 1$ V. c) Schematic of the device structure and corresponding energy band diagram of the MoTe$_2$/BN heterostructure under photodoping. MoTe$_2$ is the transport channel. BN and SiO$_2$ are the gate dielectric. BN also serves as the photosensitive medium. Si is the controlling gate. In the photodoping process, the device is under light illumination and negative backgate. The red and blue circles represent the positive charges and electrons, respectively. E_C^{BN} and E_V^{BN} represent the minimum energy of conduction band and the maximum energy of valance band of BN respectively. d) Schematic of the device structure and energy band diagram of the device after photodoping. The device is kept in the absence of external perturbation (no light and no electric field) after photodoping.

of the naturally existed bandgap in TMDs, memory device was realized by the photodoping effect in WSe$_2$/BN heterostructure, which sheds light on the logic applications.[26]

Here, we report photoinduced nonvolatile and programmable electron doping in MoTe$_2$ FET based on multilayer MoTe$_2$/BN heterostructure. The electron doping effect in MoTe$_2$ is highly robust, as reflected by its long retention time exceeding 14 d. On the other hand, the doping effect can be conveniently erased and programmed by tuning the polarity of photodoping gate exerted on BN, indicating its reversibility. Such photodoping technique coupled with its spatially controllability enables the fabrication of homogeneous MoTe$_2$ p–n junction and inverter without using photoresist as mask. The MoTe$_2$ p–n junction demonstrates an ideality factor of ≈1.13 with a current on/off ratio of ≈1.7 × 10^4, and the gain of the inverter reaches up to 98, illustrating its great potential in the application of next-generation logic electronics.

Figure 1a shows the optical microscopy image of a trilayer MoTe$_2$ FET with metal contact of Ti/Au (5 nm/80 nm), on top of the BN flake. The MoTe$_2$ and BN flakes were characterized by Raman spectra (Figure S1, Supporting Information) and atomic force microscopy (AFM) measurement (Figure S2, Supporting Information). The transfer curves ($I_{sd} - V_g$) of the MoTe$_2$ device before and after photodoping in linear scale are shown in Figure 1b. The pristine MoTe$_2$ device shows a typical hole-dominated ambipolar transport behavior, consistent with previous reports.[20] To photodope the MoTe$_2$ FET, the device is illuminated by a light pulse (duration 3 min, wavelength 405 nm, intensity 20 mW cm^{-2}) under negative photodoping gate (V_{pd}). After the photodoping process at $V_{pd} = -5$ V, the on-current in electron regime is strongly increased, which indicates an electron doping effect in the MoTe$_2$. Moreover, the on-current in electron regime almost reaches the same level as that of the hole regime, demonstrating a more symmetric and

balanced ambipolar characteristic in MoTe$_2$ device. With higher photodoping gate ($V_{pd} = -20$ V), the current of electron side is further enhanced, evolving beyond the hole side, indicating an electron-transport dominated ambipolar behavior. These results demonstrate that photodoping can effectively improve the electron transport in the MoTe$_2$ device, thereby inducing either a more balanced ambipolar or even electron-dominant transport behavior.

The mechanism of the photoinduced electron doping in the MoTe$_2$ device is shown in Figure 1c, which is proposed by the excitation of the mid-gap donor-like states (defects) in the BN flake.[25,26] It is to note that the donor-like energy levels are mainly distributed close to the middle of BN bandgap, which is illustrated by the spectra dependent characteristics in Figure S3 (Supporting Information). When the MoTe$_2$/BN heterostructure is illuminated by light, the electrons occupying the donor-like states in BN bandgap are excited to the conduction band. These photon-excited electrons can transfer into MoTe$_2$ under an external electric field (applying the negative V_{pd}), leaving positive charges localized in the mid-gap of BN. It is worth noting that the localized positive charges can weaken the external electric field exerting on BN during the doping process. The elimination of the effective electric field in BN symbolizes the termination of the doping process. The transfer curve is nearly maintained after 3 min light illumination (Figure S4, Supporting Information), suggesting the completion of the photodoping process. It is noted that the positive charges mainly distribute deep in the BN flake after photodoping,[25] which is supported by the hysteresis measurement in Figure S5 (Supporting Information). These positive charges are stored in BN even after removing the negative gate and switching off the light, which serve as an effective local gate exerting on MoTe$_2$ and results in a stable electron doping effect in MoTe$_2$ (Figure 1d). Light illumination can also induce the intrinsic photocurrent in the MoTe$_2$ flake, which is demonstrated in Figure S6 (Supporting Information). Nevertheless, such photocurrent immediately disappears once the light is off, which does not introduce any doping effect and change the transfer characteristic of the MoTe$_2$ device. The in situ Raman characterization was carried out to investigate whether other effects, such as gate-bias stress, lattice distortion, and oxidation occurred during photodoping, as shown in Figure S7 (Supporting Information). After photodoping for 3 min, we did not observe any obvious peak shift or broadening for all characteristic peaks of MoTe$_2$, and there was no additional Raman peak emerged, implying that photodoping does not introduce any additional non-negligible effects in the MoTe$_2$ flake.

The electron doping level in MoTe$_2$ can be modulated by the photodoping gate. **Figure 2**a demonstrates the evolution of transfer characteristics of MoTe$_2$ device with increasing V_{pd} from -10 to -70 V in logarithmic scale. The transfer curve of the pristine device presents a current minimum at ≈ 4 V. As V_{pd} gradually increases to -70 V, the current minimum progressively moves to ≈ -70 V. This suggests a significant gate-tunable electron doping effect in MoTe$_2$. To quantitatively evaluate the effectiveness of the doping process, we extract the electron concentration (n_e) in the linear transport regime after photodoping under different V_{pd} using Equation (1)[27]

$$n = -\frac{C_g(V_g - V_{th})}{e} \tag{1}$$

where C_g is the capacitance per unit area for the back gate, comprising of 300 nm SiO$_2$ and 14.5 nm BN, $\approx 1.1 \times 10^{-8}$ F cm^{-2}. V_{th} is the threshold voltage for electron transport. Figure 2b shows the electron concentration at $V_g = 40$ V as a function of V_{pd}. In the pristine MoTe$_2$ device, the electron concentration is derived to be 2.9×10^{11} cm^{-2}, which increases to 5.8×10^{11} cm^{-2} after photodoping under $V_{pd} = -10$ V. With further increasing the V_{pd} to -70 V, the electron concentration is largely increased to 2.8×10^{12} cm^{-2}, nearly tenfold that of the pristine MoTe$_2$. The larger V_{pd} facilitates the formation of higher concentration of localized positive charges in BN, which induces more effective electron-doping and greater electron concentration in the MoTe$_2$ device. The electron mobility (μ_e) with respect to V_{pd} is also investigated and plotted in Figure 2b. The field effect electron mobility is calculated using Equation (2)

$$\mu = \frac{L}{W C_g V_{sd}} \frac{dI_{sd}}{dV_g} \tag{2}$$

where dI_{sd}/dV_g represents the slope extracted from the linear regime of the electron transport, L and W are the length and width of the conduction channel respectively. Intriguingly, the photodoped MoTe$_2$ device demonstrates a strong enhancement of electron mobility, from 1.1 cm^2 V^{-1} s^{-1} for pristine MoTe$_2$ to 10.2 cm^2 V^{-1} s^{-1} after doping at $V_{pd} = -70$ V. We propose that the mobility enhancement is mainly due to the reduction of Schottky barrier width between MoTe$_2$ and metal contacts after photodoping.[10,13] The electron doping pulls MoTe$_2$ Fermi level toward its conduction band, which reduces the Schottky barrier width for electron injection, thereby leading to the improved electron mobility. The I_{sd}–V_{sd} output curves become much more linear at the low V_{sd} regime and demonstrate near-ideal ohmic behavior after photodoping, as shown in Figure S8 (Supporting Information), which suggests the reduction of the contact resistance as well as the Schottky barrier width for electron transport.[10,13]

Nonvolatility is an important feature in doping technique, which allows the retention of doping effect in doped material in the absence of external perturbation. Figure 2c exhibits the evolution of transfer characteristics of the doped MoTe$_2$ device ($V_{pd} = -70$ V) as prolonging the retention time up to 14 d. The on-state current in the electron regime is retained with only slight decline, and the current minimum demonstrates weak shift after two weeks. The electron concentration and mobility were extracted and plotted as a function of retention time in Figure 2d, where these two parameters nearly remain unchanged over 14 d. The transfer characteristics at $V_{pd} = -10$, -30, and -50 V were also investigated, demonstrating the similar retention behavior (Figure S9, Supporting Information). These results illustrate an outstanding nonvolatility property of the photodoped MoTe$_2$ device. The long retention time in the MoTe$_2$ device can be attributed to two factors, namely, the highly localized positive charges in BN after doping, and the potential barrier between MoTe$_2$ and BN. The positive charges in BN serve as a highly stable local gate to maintain the electron doping in MoTe$_2$. In addition, due to the high potential barrier
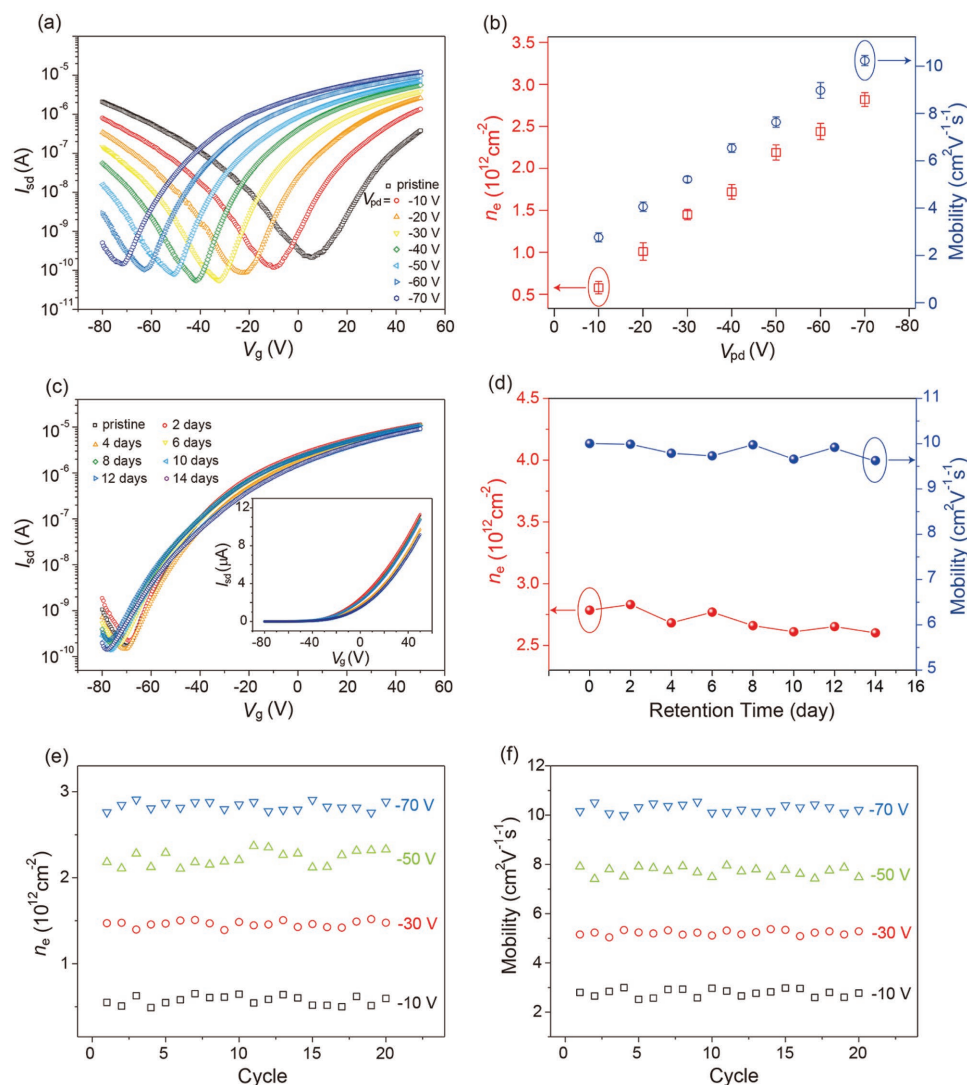
Figure 2. a) Transfer characteristics evolution of the MoTe$_2$ device as increasing V_{pd} from −10 to −70 V with 10 V step. b) Electron concentration (n_e) at $V_g = 40$ V and electron mobility of MoTe$_2$ versus V_{pd}. The error bars are defined by the errors from the 20 independent photodoping cycles. c) Transfer characteristics evolution in both logarithmic and linear scale (inset) as prolonging retention time to 14 d after photodoping at $V_{pd} = −70$ V. The device is kept in dark condition without electric field, and the transfer measurement was taken every 2 d. d) Plot of electron concentration and mobility with respect to the retention time. e,f) Cycling test for electron concentration (e) and mobility (f) at four different photodoping gates ($V_{pd} = −10, −30, −50, −70$ V).

between BN and MoTe$_2$, the electrons in MoTe$_2$ are unable to transfer back into BN without external assistance (e.g., external electric field and light illumination), thus reducing the possibility of charge recombination. This ensures the stability of the positive charges in BN and the long retention time of the doped MoTe$_2$ device.

In addition to nonvolatility, programmability is another important characteristic which enables the flexible fabrication of logic devices. The electron doping effect in MoTe$_2$ can be erased, indicating the programmable nature of the photodoping technique. The erasing operation is realized by applying positive gate on the MoTe$_2$/BN heterostructure under light illumination, as shown in Figure S10a (Supporting Information). In this process, the ionized positive defects in BN are filled by photon-excited electrons from BN valence band, generating large quantity of holes. Attributing to the external electric field, the

generated holes in BN move to MoTe$_2$. Consequently, the localized positive charges in BN are vanished and the device returns to its original transport behavior after erasing (Figure S10b, Supporting Information). Figure 2e,f display the repeatability of electron concentration and mobility at different $V_{pd} = −10, −30, −50,$ and $−70$ V for 20 dope/erase cycles, respectively. The electron concentration and mobility only fluctuate slightly through the 20 cycles at different V_{pd}. The deviations from the average values of the electron concentration and mobility for each V_{pd} are less than 15%, demonstrating the excellent programmability of the photodoped MoTe$_2$ device.

The photoinduced electron doping in MoTe$_2$ provides the opportunity to fabricate homogeneous p–n junction and inverter with arbitrary doping pattern. More importantly, unlike the traditional SCTD technique which requires photolithography together with photoresist to spatially control the

**ADVANCED
SCIENCE NEWS**

www.advancedsciencenews.com

**ADVANCED
MATERIALS**

www.advmat.de

doping profile of TMDs,[19,20] the realization of homogeneous p–n junction and inverter employing photodoping technique is photoresist-free, since the TMDs can be selectively doped through controlling the TMDs/BN heterostructure configuration or light illumination region. To confirm our hypothesis, the scanning kelvin probe microscopy (SKPM) measurements were carried out for the pristine and photodoped $MoTe_2$ flake with half located on BN and another half on SiO_2, as shown in **Figure 3**a. The SKPM measurements were performed using Bruker Dimension Icon SPM in PeakForce Tapping Mode through highly doped Si tips (PFQNE-AL) in ambient condition. Figure 3b exhibits the AFM height image of the heterostructure, with BN thickness around ≈14.2 nm. The SKPM image of

pristine $MoTe_2$ flake (before photodoping) is demonstrated in Figure 3c. The contact potential difference (CPD) between the sample and the AFM tip in the SKPM image is given by

$$CPD = \frac{(\Phi_{sample} - \Phi_{tip})}{e} \tag{3}$$

where Φ_{sample} and Φ_{tip} are the work function of the sample and the tip, respectively. e is the elementary charge. The CPD difference of the $MoTe_2$ flakes on SiO_2 and BN substrates is around ≈27 mV before photodoping (Figure 3d), which is possibly due to the interface trap charges on SiO_2 substrate. After photodoping at $V_{pd} = -50$ V for 3 min (405 nm light with
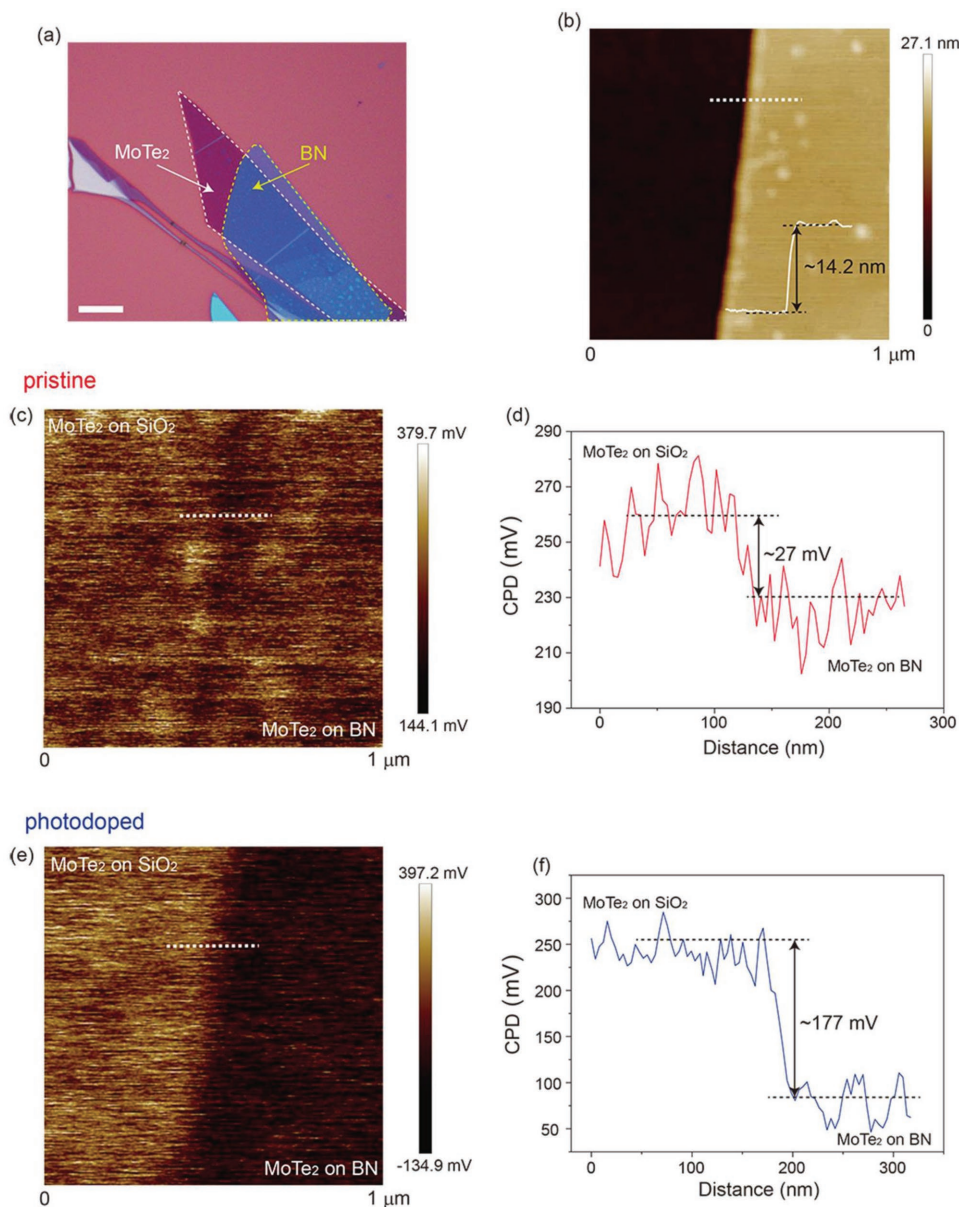

Figure 3. a) Optical image of $MoTe_2$/BN heterostructure. The scale bar is 10 µm. b) AFM image of the $MoTe_2$ flake. Half $MoTe_2$ is on SiO_2, with another half on h-BN flake. Inset: AFM line profile of the $MoTe_2$ on SiO_2 and h-BN. c,e) SKPM images of $MoTe_2$ flake before (c) and after (e) photodoping at $V_{pd} = -50$ V. e,f) The line scans, denoted by the white dotted lines in the $MoTe_2$ SKPM images before (d) and after (f) photodoping.

1804470 (5 of 9)

intensity of ≈ 20 mW cm^{-2}), the CPD of the MoTe$_2$ flake on SiO$_2$ is almost unchanged, while the CPD of the MoTe$_2$ flake on BN demonstrates a remarkable reduction by nearly ≈ 150 mV (Figure 3e,f). This indicates that the Fermi level of the photo-doped MoTe$_2$ moves closer to its conduction band, revealing an increase of electron concentration and the n-type doping effect in the photodoped MoTe$_2$, in good agreement with the device measurement results as discussed in Figure 2. Moreover, the potential difference of the MoTe$_2$ flakes on SiO$_2$ and BN substrates reaches up to ≈ 177 mV after photodoping, revealing an obvious band bending and the generation of MoTe$_2$ homojunction at the SiO$_2$/BN interface. The potential difference is much larger than that of the WSe$_2$ homojunction (≈ 55 mV) achieved by helium ion irradiation,[28] and comparable to that of the CVD grown WS$_2$/WSe$_2$ heterostructure (≈ 113 mV),[29] as well as the lateral WSe$_2$ junction (≈ 200 mV) achieved by H$_2$ plasma treatment induced degenerated n-type doping.[30]

Figure 4a shows the schematic of a homogeneous MoTe$_2$ p–n junction achieved by controlling the MoTe$_2$/BN heterostructure configuration. Half of the MoTe$_2$ flake is transferred on BN substrate, with another half on SiO$_2$. During the photodoping process, the MoTe$_2$ flake on BN is electron-doped, while the flake on SiO$_2$ retains its hole-dominated transport behavior, thereby forming a nonvolatile homogeneous p–n junction at the homointerface. Figure 4b exhibits the optical microscopy image of the MoTe$_2$ p–n junction. To realize the steep p–n homojunction, the device was photodoped under $V_{pd} = -50$ V. Figure 4c exhibits the typical rectification characteristics ($I_{sd}-V_{sd}$) of the

MoTe$_2$ diode under gate voltage from -65 to -51 V with 2 V step in linear and logarithmic (inset) scale. As V_g increases from -65 to -57 V, the currents in both the negative and positive bias regimes decline rapidly. Note that the current at the negative bias drops much faster than that at the positive side, thereby yielding a remarkable improvement of the rectification ratio (the ratio between the forward current at $V_{sd} = 2$ V and the reverse current at $V_{sd} = -2$ V). When further increasing V_g from -57 to -51 V, the forward current continues to decrease while the reverse current almost keeps unchanged, resulting in a decline of the rectification ratio. As shown in Figure S11a (Supporting Information), the rectification ratio experiences a significant enhancement when increasing V_g from -65 to -57 V, peaking at 1.7×10^4, followed by a gradual decrease. The gate dependent rectification behavior is mainly attributed to the tunability of the built-in potential barrier across the photodoped and undoped MoTe$_2$ boundary by applying external electric field. As shown in Figure S11b,c (Supporting Information), the homogeneous junction of the half-doped MoTe$_2$ junction evolves from p–p, across p–n, and finally to n–n when positively sweeping the back gate, consistent with previous reports in black phosphorus devices.[31,32]

The $I_{sd}-V_{sd}$ at $V_g = -53$ V in both linear and logarithmic scale is plotted in Figure 4d. The reverse current is as low as $\approx 10^{-11}$ A, representing the promising characteristic for low-power electronics. When the bias is switched to the positive regime, the current demonstrates a sharp increase up to $\approx 10^{-7}$ A, which is a hallmark of diode behavior. By linear fitting the current onset
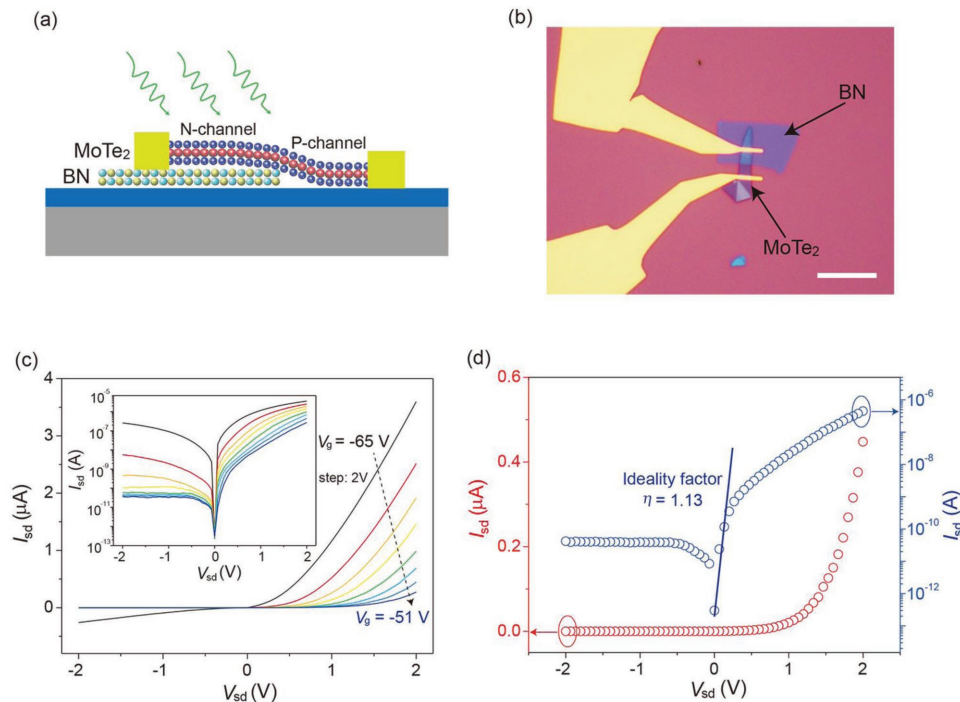

Figure 4. a) Schematic illustration of the homogeneous MoTe$_2$ p–n junction achieved by controlling the MoTe$_2$/BN heterostructure configuration. The left MoTe$_2$ channel on BN is electron doped, while the right channel on SiO$_2$ retains original hole-dominated transport behavior. b) Optical microscopy image of the fabricated MoTe$_2$ p–n junction. Half MoTe$_2$ flake is on BN with another half on SiO$_2$. The scale bar is 10 μm. c) The $I_{sd}-V_{sd}$ characteristics (V_{sd} from -2 to 2 V) of the MoTe$_2$ p–n junction in both linear and logarithmic scale (inset) at $V_{pd} = -50$ V. The rectifying behavior of the MoTe$_2$ diode is tunable by backgate V_g after photodoping. The V_g is tuned from -65 to -51 V with 2 V step. d) The rectification characteristic of the MoTe$_2$ diode at $V_g = -53$ V in both linear and logarithmic scale.

**ADVANCED
SCIENCE NEWS**

www.advancedsciencenews.com
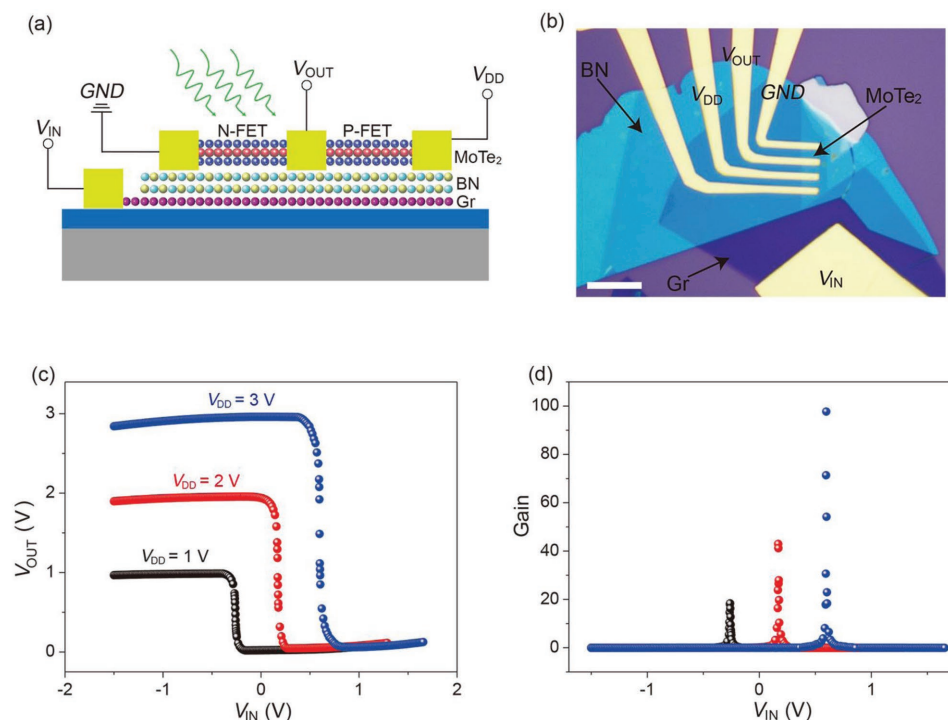
**ADVANCED
MATERIALS**

www.advmat.de

Figure 5. a) Schematic illustration of the homogeneous MoTe$_2$ inverter achieved by controlling the light illumination region. Graphene (Gr) is the controlling gate, which also provides the input signal. BN serves as the gate dielectric and photosensitive medium. MoTe$_2$ is the transport channel with three planar electrodes which serve as V_{DD}, V_{OUT}, and ground (GND), respectively. The left MoTe$_2$ channel is illuminated by a fine-focused laser beam under negative backgate, while the right channel is left unilluminated. b) Optical microscopy image of the MoTe$_2$ inverter. Graphene was exfoliated on SiO$_2$/Si substrate, followed by the transfer of BN and MoTe$_2$ flakes. The scale bar is 10 μm. c) The output characteristic of the MoTe$_2$ inverter at V_{DD} = 1, 2, and 3 V, respectively. The output curves are clearly divided in three regimes, that is, the "high state" for high V_{OUT}, "steep slope" for the sharp decrease of V_{OUT}, and "low state" for low V_{OUT}, a hall mark of inverter behavior. d) The extracted gains of the inverter as a function of input voltage. The highest gains at V_{DD} = 1, 2, and 3 V are 18, 42, and 98, respectively.

in logarithm scale,[12,31,32] the ideality factor η is extracted to be ≈1.13, exhibiting a near-ideal p–n junction. Such near-ideal MoTe$_2$ diode coupling with the large rectification ratio indicates the great potential of the photodoping technique in high performance and photoresist-free TMDs p–n junction.

In addition to p–n junction, homogeneous MoTe$_2$ inverter can also be achieved by spatially controlling the doping of MoTe$_2$ channel using photodoping technique. **Figure 5**a shows the schematic of the MoTe$_2$ inverter with two channels in series. Through controlling the light illumination region, the two channels can be selectively doped. The left channel presents n-type transport behavior after photodoping, while the right channel retains its original p-type transport. The three metal contacts on MoTe$_2$ sequentially serve as ground GND, output signal V_{OUT}, and power supply V_{DD}, respectively. To improve the performance of the inverter, few-layer graphene (Gr) is used as the bottom gate to provide the input signal V_{IN}. Figure 5b shows the optical microscopy image of the fabricated MoTe$_2$ inverter. The device is nearly free of interfacial bubbles and residues after the dry transfer processes (Figure S12, Supporting Information), indicating the high quality of the inverter with clean interfaces. A fine-focused laser beam with spot diameter ≈3 μm was used to spatially control the doping of the MoTe$_2$ channel. As shown in the transfer characteristics in Figure S13 (Supporting Information), the electron transport in the doped MoTe$_2$ channel (at V_{pd} = −1 V) is significantly

enhanced, while the undoped MoTe$_2$ preserves hole-dominated transport behavior. Figure 5c shows the output characteristic of the homogeneous MoTe$_2$ inverter as a function of V_{IN} at V_{DD} = 1 V, 2 V, and 3 V respectively. The output curves are clearly divided into three demonstrative regimes of an inverter: the "high state" for high V_{OUT}, "steep slope" for the sharp decrease of V_{OUT}, and "low state" for low V_{OUT}. To evaluate the performance of the inverter, the gain is extracted from the slope of the output characteristic (gain = dV_{OUT}/dV_{IN}) at the three different V_{DD} (Figure 5d). The gain follows a Dirac-δ function with respect to the V_{IN}, in which the highest value occurs at the steepest region in the output curve. The gain reaches up to 18 at small V_{DD} = 1 V. With further increasing the V_{DD} to 2 and 3 V, the gain is remarkably enhanced to 42 and 98, respectively, which is among the highest values reported for 2D-material-based homoinverters.[33,34] The subthreshold swings of the undoped and doped MoTe$_2$ channels are as small as 178 and 126 mV dec^{-1} respectively, ensuring the fast switching between the high state and low state for the MoTe$_2$ inverter with the high gain.[33,35] Static power consumption is another important factor for complementary inverter, which is exhibited in Figure S14 (Supporting Information). The static power consumption gradually decreases with reducing V_{DD}, from several μW at V_{DD} = 3 V to several tens of pW at V_{DD} = 0.1 V. It is noted that the power consumption can be as low as 370 pW when V_{DD} is reduced to 0.1 V, which is comparable to other TMDs-based inverters.[33]

**ADVANCED
SCIENCE NEWS**
www.advancedsciencenews.com

**ADVANCED
MATERIALS**
www.advmat.de

In summary, we have demonstrated photoinduced electron doping in $MoTe_2$ device based on the $MoTe_2$/BN heterostructure configuration. The photon-generated electrons from the mid-gap donor-like states in BN transfer into $MoTe_2$ under negative gate, leading to the storage of localized positive charges in BN bandgap. These positive charges can serve as effective local gate, which results in the electron doping effect in $MoTe_2$. Such doping effect can be erased by tuning the polarity of the photodoping gate under light illumination. In the erasing process, the localized positive charges stored in BN recombine with the photoexcited electrons from the BN valence band, thereby eliminating the local gating effect and restoring the original transport behavior of $MoTe_2$. The photodoping effect has been written and erased for 20 cycles with only slight deviation of the electron transport behavior between each cycle, suggesting the excellent repeatability. On the other hand, in the absence of external perturbation, the photodoping effect in $MoTe_2$ is retained for over 14 d, illustrating its robust nonvolatility. Moreover, the electron transport properties, including the electron concentration and mobility in $MoTe_2$ device, can be precisely modulated through adjusting the photodoping gate. The electron doping profile in $MoTe_2$ device can also be spatially controlled, making it possible to fabricate homogeneous p–n junction and inverter. The $MoTe_2$ p–n junction is realized by configuring the $MoTe_2$/BN heterostructure, in which the diode exhibits a near-unity ideality factor of ≈1.13 with a rectification ratio of ≈1.7×10^4. On the other hand, through controlling the illumination region on the $MoTe_2$ channel, the $MoTe_2$ inverter is achieved with a remarkable gain of ≈98 at $V_{DD} = 3$ V. The discovery of photodoping technique in 2D TMDs provides a simple method to achieve TMDs-based nonvolatile and programmable complementary electronic devices in high performance, which paves the way for the application of 2D TMDs in future photoresist-free logic electronics.

Experimental Section

Fabrication of 2D $MoTe_2$/BN and $MoTe_2$/BN/Graphene Heterostructure: The hybrid structure of $MoTe_2$ and BN was achieved by a dry transfer method in a glove box (Ar atmosphere).[36] First, few-layer BN flake was mechanically exfoliated onto 300 nm SiO_2/Si substrate. In the following, the $MoTe_2$ flake exfoliated on a transparent polydimethylsiloxane (PDMS) substrate was aligned on the BN flake using optical microscope. After the alignment, the PDMS film was pressed on the Si substrate for ≈2 min followed by a slow lift up, during which the $MoTe_2$ flake was transferred onto the BN flake. The $MoTe_2$/BN/graphene heterostructure was fabricated by the same method in the glove box. Graphene flake was exfoliated on SiO_2/Si substrate first, followed by the dry transfer of BN and $MoTe_2$ flakes in sequence. After the dry transfer, the $MoTe_2$/BN or $MoTe_2$/BN/graphene heterostructures on SiO_2/Si substrate was spin-coated by PMMA in the same glove box for device fabrication. The electrodes were patterned by standard electron beam lithography (EBL) in high vacuum (≈10^{-6} mbar), followed by the development in MIBK/IPA (1:3) solution in the glove box. The sample was then loaded in a thermal evaporator in high vacuum (≈10^{-7} mbar) to deposit metal contacts of Ti/Au (5 nm/80 nm). After that, the sample was immersed in acetone solution for several hours to lift off the PMMA layer in the glove box. After liftoff, the as-made devices were wire-bonded onto a leaded chip carrier (LCC) in air immediately, then loaded in a custom-designed high vacuum chamber (≈10^{-7} mbar).

Electrical Characterization of the 2D FET, p–n Junction, and Inverter: All the devices were characterized in a high vacuum chamber (≈10^{-7} mbar).

All the fabricated devices were also stored in the high vacuum chamber after measurements. The electrical measurements were conducted by using an Agilent 2912A source measure unit. A microsized laser beam with wavelength 405 nm was used to modulate the photodoping effect. The light intensity of laser beam was calibrated by THORLABS GmbH (PM 100A) power meter.

Supporting Information

Supporting Information is available from the Wiley Online Library or from the author.

Conflict of Interest

The authors declare no conflict of interest.

[1] Q. H. Wang, K. Kalantar-Zadeh, A. Kis, J. N. Coleman, M. S. Strano, *Nat. Nanotechnol.* **2012**, *7*, 699.

[2] K. F. Mak, C. Lee, J. Hone, J. Shan, T. F. Heinz, *Phys. Rev. Lett.* **2010**, *105*, 136805.

[3] H. Liu, A. T. Neal, P. D. Ye, *ACS Nano* **2012**, *6*, 8563.

[4] G.-H. Lee, Y.-J. Yu, X. Cui, N. Petrone, C.-H. Lee, M. S. Choi, D.-Y. Lee, C. Lee, W. J. Yoo, K. Watanabe, T. Taniguchi, C. Nuckolls, P. Kim, J. Hone, *ACS Nano* **2013**, *7*, 7931.

[5] H. Wang, L. Yu, Y.-H. Lee, Y. Shi, A. Hsu, M. L. Chin, L.-J. Li, M. Dubey, J. Kong, T. Palacios, *Nano Lett.* **2012**, *12*, 4674.

[6] D. Akinwande, N. Petrone, J. Hone, *Nat. Commun.* **2014**, *5*, 5678.

[7] Y. H. Lee, X. Q. Zhang, W. Zhang, M. T. Chang, C. T. Lin, K. D. Chang, Y. C. Yu, J. T. W. Wang, C. S. Chang, L. J. Li, T. W. Lin, *Adv. Mater.* **2012**, *24*, 2320.

[8] Y. Shi, H. Li, L.-J. Li, *Chem. Soc. Rev.* **2015**, *44*, 2744.

[9] Y. Gong, H. Yuan, C.-L. Wu, P. Tang, S.-Z. Yang, A. Yang, G. Li, B. Liu, J. van de Groep, M. L. Brongersma, M. F. Chisholm, S. C. Zhang, W. Zhou, Y. Cui, *Nat. Nanotechnol.* **2018**, *13*, 294.

[10] H. Fang, M. Tosun, G. Seol, T. C. Chang, K. Takei, J. Guo, A. Javey, *Nano Lett.* **2013**, *13*, 1991.

[11] M. Tosun, S. Chuang, H. Fang, A. B. Sachid, M. Hettick, Y. Lin, Y. Zeng, A. Javey, *ACS Nano* **2014**, *8*, 4948.

ADVANCED
SCIENCE NEWS

www.advancedsciencenews.com

ADVANCED
MATERIALS

www.advmat.de

[12] D. Qu, X. Liu, M. Huang, C. Lee, F. Ahmed, H. Kim, R. S. Ruoff, J. Hone, W. J. Yoo, *Adv. Mater.* **2017**, *29*, 1606433.

[13] D. Kiriya, M. Tosun, P. Zhao, J. S. Kang, A. Javey, *J. Am. Chem. Soc.* **2014**, *136*, 7853.

[14] L. Yang, K. Majumdar, H. Liu, Y. Du, H. Wu, M. Hatzistergos, P. Hung, R. Tieckelmann, W. Tsai, C. Hobbs, P. D. Ye, *Nano Lett.* **2014**, *14*, 6275.

[15] J. D. Lin, C. Han, F. Wang, R. Wang, D. Xiang, S. Qin, X.-A. Zhang, L. Wang, H. Zhang, A. T. S. Wee, W. Chen, *ACS Nano* **2014**, *8*, 5323.

[16] Z. Hu, Z. Wu, C. Han, J. He, Z. Ni, W. Chen, *Chem. Soc. Rev.* **2018**, *47*, 3100.

[17] S. Lei, X. Wang, B. Li, J. Kang, Y. He, A. George, L. Ge, Y. Gong, P. Dong, Z. Jin, G. Brunetto, W. Chen, Z. T. Lin, R. Baines, D. S. Galvao, J. Lou, E. Barrera, K. Banerjee, R. Vajtai, P. Ajayan, *Nat. Nanotechnol.* **2016**, *11*, 465.

[18] B. Lei, Y. Pan, Z. Hu, J. Zhang, D. Xiang, Y. Zheng, R. Guo, C. Han, L. Wang, J. Lu, L. Yang, W. Chen, *ACS Nano* **2018**, *12*, 2070.

[19] J. Y. Lim, A. Pezeshki, S. Oh, J. S. Kim, Y. T. Lee, S. Yu, D. K. Hwang, G. H. Lee, H. J. Choi, S. Im, *Adv. Mater.* **2017**, *29*, 1701798.

[20] W. Luo, M. Zhu, G. Peng, X. Zheng, F. Miao, S. Bai, X. A. Zhang, S. Qin, *Adv. Funct. Mater.* **2018**, *28*, 1704539.

[21] A. Pospischil, M. M. Furchi, T. Mueller, *Nat. Nanotechnol.* **2014**, *9*, 257.

[22] J. S. Ross, P. Klement, A. M. Jones, N. J. Ghimire, J. Yan, D. Mandrus, T. Taniguchi, K. Watanabe, K. Kitamura, W. Yao, D. H. Cobden, X. D. Xu, *Nat. Nanotechnol.* **2014**, *9*, 268.

[23] B. W. Baugher, H. O. Churchill, Y. Yang, P. Jarillo-Herrero, *Nat. Nanotechnol.* **2014**, *9*, 262.

[24] Y.-Q. Bie, G. Grosso, M. Heuck, M. M. Furchi, Y. Cao, J. Zheng, D. Bunandar, E. Navarro-Moratalla, L. Zhou, D. K. Efetov, T. Taniguchi, K. Watanabe, J. Kong, D. Englund, P. Jarillo-Herrero, *Nat. Nanotechnol.* **2017**, *12*, 1124.

[25] L. Ju, J. Velasco Jr., E. Huang, S. Kahn, C. Nosiglia, H.-Z. Tsai, W. Yang, T. Taniguchi, K. Watanabe, Y. Zhang, G. Zhang, M. Crommie, A. Zettl, F. Wang, *Nat. Nanotechnol.* **2014**, *9*, 348.

[26] D. Xiang, T. Liu, J. Xu, J. Y. Tan, Z. Hu, B. Lei, Y. Zheng, J. Wu, A. C. Neto, L. Liu, W. Chen, *Nat. Commun.* **2018**, *9*, 2966.

[27] D. Xiang, C. Han, J. Wu, S. Zhong, Y. Liu, J. Lin, X.-A. Zhang, W. P. Hu, B. Özyilmaz, A. C. Neto, A. T. S. Wee, W. Chen, *Nat. Commun.* **2015**, *6*, 6485.

[28] M. G. Stanford, P. R. Pudasaini, A. Belianinov, N. Cross, J. H. Noh, M. R. Koehler, D. Mandrus, G. Duscher, A. J. Rondinone, I. N. Ivanov, T. Z. Ward, P. D. Rack, *Sci. Rep.* **2016**, *6*, 27276.

[29] B. Zheng, C. Ma, D. Li, J. Lan, Z. Zhang, X. Sun, W. Zheng, T. Yang, C. Zhu, G. Ouyang, G. Xu, X. Zhu, X. Wang, A. Pan, *J. Am. Chem. Soc.* **2018**, *140*, 11193.

[30] M. Tosun, L. Chan, M. Amani, T. Roy, G. H. Ahn, P. Taheri, C. Carraro, J. W. Ager, R. Maboudian, A. Javey, *ACS Nano* **2016**, *10*, 6853.

[31] G. Wang, L. Bao, T. Pei, R. Ma, Y.-Y. Zhang, L. Sun, G. Zhang, H. Yang, J. Li, C. Gu, H. Yang, J. Li, C. Gu, S. Du, S. T. Pantelides, R. D. Schrimpf, H. J. Gao, *Nano Lett.* **2016**, *16*, 6870.

[32] C. Han, Z. Hu, L. C. Gomes, Y. Bao, A. Carvalho, S. J. Tan, B. Lei, D. Xiang, J. Wu, D. Qi, L. Wang, F. Huo, W. Huang, K. P. Loh, W. Chen, *Nano Lett.* **2017**, *17*, 4122.

[33] J. Pu, K. Funahashi, C. H. Chen, M. Y. Li, L. J. Li, T. Takenobu, *Adv. Mater.* **2016**, *28*, 4111.

[34] S. P. Koenig, R. A. Doganov, L. Seixas, A. Carvalho, J. Y. Tan, K. Watanabe, T. Taniguchi, N. Yakovlev, A. H. Castro Neto, B. Ozyilmaz, *Nano Lett.* **2016**, *16*, 2145.

[35] M. Huang, S. Li, Z. Zhang, X. Xiong, X. Li, Y. Wu, *Nat. Nanotechnol.* **2017**, *12*, 1148.

[36] A. Castellanos-Gomez, M. Buscema, R. Molenaar, V. Singh, L. Janssen, H. S. J. van der Zant, G. A. Steele, *2D Mater.* **2014**, *1*, 011002.